Revista Mexicana de Astronomía y Astrofísica, **56**, 179–191 (2020)

https://doi.org/10.22201/ia.01851101p.2020.56.02.01

γ DOR: A PULSATING COMPONENT OF KIC 8043961 IN A STELLAR TRIPLE SYSTEM

C. Kamil, H. A. Dal, O. Özdarcan, and E. Yoldaş

Department of Astronomy and Space Sciences, University of Ege, İzmir, Turkey.

Received February 5 2018; accepted April 20 2020

ABSTRACT

We present new findings about KIC 8043961. We find the effective temperatures of the components as 6900 ± 200 K for the primary, and 6598 ± 200 K for the secondary, while the logarithm of the surface gravities are found to be 4.06 cm s^{-2} and 3.77 cm s^{-2}, respectively. Combination of the light curve with the spectroscopic orbit model results leads to a mass ratio of 1.09 ± 0.07 with an orbital inclination of 73.71 ± 0.14 and a semi-major axis of $8.05 \pm 0.22\,R_\odot$. Masses of the primary and secondary components are calculated as $1.379 \pm 0.109\,M_\odot$ and $1.513 \pm 0.181\,M_\odot$, while the radii are found to be $1.806 \pm 0.084\,R_\odot$ and $2.611 \pm 0.059\,R_\odot$. In addition, we obtain a considerable light contribution ($\approx$0.54%) of a third body. We compute a possible mass for the third body as $0.778 \pm 0.002\,M_\odot$. We find that the primary component exhibits γ Dor type pulsations with 137 frequencies.

RESUMEN

Presentamos nuevos hallazgos sobre KIC 8043961. Encontramos que la temperatura efectiva es de 6900 ± 200 K para la primaria, y de 6598 ± 200 K para la secundaria, mientras que los logaritmos de las gravedades superficiales son, respectivamente, 4.06 cm s^{-2} y 3.77 cm s^{-2}. Combinamos la curva de luz con un modelado espectroscópico de la órbita y obtenemos un cociente de masas de 1.09 ± 0.07, una inclinación orbital de 73.71 ± 0.14 y un semieje mayor de $8.05 \pm 0.22\,R_\odot$. Calculamos las masas de la primaria y de la secundaria, y obtenemos $1.379 \pm 0.109\,M_\odot$ y $1.513 \pm 0.181\,M_\odot$. Los radios son, respectivamente, $1.806 \pm 0.084\,R_\odot$ y $2.611 \pm 0.059\,R_\odot$. Además encontramos una contribución apreciable de un tercer cuerpo, ($\approx 0.54\%$). Calculamos la masa posible del tercer cuerpo y obtenemos $0.778 \pm 0.002\,M_\odot$. Encontramos que la primaria muestra pulsaciones tipo γ Dor con 137 frecuencias.

Key Words: techniques: photometric — methods: data analysis — stars: binaries: eclipsing — stars: individual: γ Dor, KIC 8043961

1. INTRODUCTION

Astronomers have been trying to find a better way to understand stellar evolution in detail. Like the Kepler Mission, the space missions have been giving a new perspective on this point, as expected. For instance, the Kepler Mission first aimed to detect exo-planets (Borucki et al. 2010; Koch et al. 2010; Caldwell et al. 2010). For this aim, scientists counted on its highest quality and sensitivity ever obtained in the photometry (Jenkins et al. 2010a,b). Indeed, the high quality data accumulated by the Kepler Satellite revealed the presence of numerous variable targets, such as new eclipsing binaries, apart from discovering thousands of exo-planets (Slawson et al. 2011; Matijevič et al. 2012). Many of the newly discovered eclipsing binaries possess chromospherically active components (Balona 2015), while lots of them have pulsating components with several frequencies (Kamil and Dal 2017; Özdarcan and Dal 2017).

Stellar pulsation is an important phenomenon to understand stellar evolution. On this point, the very high precision photometry of the Kepler Satellite provides a remarkable chance to astronomers. Before the space missions, the photometric observations revealed the presence of several types of pulsating stars, such as γ Doradus, δ Scuti type pulsat-

TABLE 1

LITERATURE PARAMETERS FOR THE TARGET

T (K)	$\log(g)$ (cms^{-2})	R ($R_\odot$)	M ($M_\odot$)	[Fe/H]	Ref
6565	-	-	-	0.270	Ammons et al. (2006)
6348-6666	3.620	-	-	−0.380	Pinsonneault et al. (2012)
6657	3.621	3.177	1.532	−0.375	Huber et al. (2014)
6626-6935	4.100	-	-	−0.130	Frasca et al. (2016)
6649	3.619	3.177	1.532	−0.380	Mathur et al. (2017)

ing, and also solar-like oscillating stars on the main sequence of the Hertzsprung-Russell (hereafter HR) diagram. Although there are several types of pulsating stars out of the main sequence, these samples are located close to the main sequence, sometimes side by side. In addition, the physical processes behind the pulsating nature of these stars are easily demonstrated by astroseismology, depending on the analysis of the pulsation frequencies. This is why the pulsating stars play a key role to understand stellar evolution (Cunha et al. 2007; Aerts et al. 2010).

Recent studies in the literature demonstrated that some stars can pulsate in both pressure (p) and gravity (g) modes. These stars are generally classified as γ Dor / δ Scuti hybrid pulsators. It is well known that p-modes, which are observed in the δ Scuti type variables, are generally sensitive to the outer layers of the star, while g-modes, which are observed in the γ Doradus type stars, are sensitive to the stellar interior (Aerts et al. 2010). After analyzing data obtained by the Kepler Satellite, the number of hybrid pulsators has remarkably increased (Grigahcéne et al. 2010; Uytterhoeven et al. 2011; Tkachenko et al. 2013; Balona 2014).

One of such systems worth examining is KIC 8043961 (Kirk et al. 2016), on which nature there are several debates. Although there are several studies on KIC 8043961, they are generally grouped into two areas, such as temperature and triplicity. Ammons et al. (2006) computed the target $E(B-V)$ as $0^m.023$ for its estimated distance of 76 pc. According to Pickles and Depagne (2010), KIC 8043961 is a main sequence source of spectral type F6, while Watson et al. (2006) listed the target as a variable star with a period of 1.559231 d. They also gave the stellar distance as 589.757 pc depending on $A_v = 0^m.358$. Frasca et al. (2016) indicated that the target was a main sequence source with a spectral type of F0-F2. Some physical parameters given in the literature are listed in Table 1 and, as seen from the table, the physical nature of system is not absolutely determined. The most important study about KIC 8043961 is that of Conroy et al. (2014), where they posited a third body in an almost circular orbit with period of 478 day, depending on the eclipse time variation, and an amplitude of 184 s. Recently, Borkovits et al. (2016) also found a variation with a period of 478.6 d from the eclipse times. Taking the total mass as $\approx 2M_\odot$ for the eclipsing binary, they estimated a minimum mass of 0.61 $M_\odot$ for the third body, with $e = 0.247$ and $\omega = 13$ degree.

In this study, we try to reveal the nature of KIC 8043961, separately analyzing each variation detected in its light curve together with spectroscopic observations. In the next section, we summarize the observations and data reductions. Then, we determine the radial velocity variation from the available spectroscopic observations in § 3.1; we estimate the temperatures of the components from the same observations in § 3.2. To determine the size of the third body, we examine the $O-C$ variation in § 3.3, and we model the light curve of the eclipsing binary in § 3.4. In § 3.5 we further analyse the out-of-eclipse variations. We summarize and discuss our findings in the last section.

2. OBSERVATIONS AND DATA REDUCTIONS

2.1. *Spectral Observation*

We carried out spectroscopic observations of the system with the 1.5-m Russian - Turkish telescope and the Turkish Faint Object Spectrograph Camera (TFOSC[1]) at Tubitak National Observatory. Using the échelle mode of TFOSC, we achieve an actual resolution of R=$\lambda/\Delta\lambda \approx 3000$ around 5500Å. The whole spectrum covers a wavelength interval between 3900 - 9100Å in 11 échelle orders. All spectra were recorded with a back illuminated 2048 × 2048 pixels CCD camera, which has a pixel size of 15 × 15 μm^2.

We recorded eight optical spectra of KIC8043961 between the 2014 and 2017 observing seasons. In addition, we obtained optical spectra of ι Psc (HD 222368, F7V, $v_r = 5.656$ kms^{-1}) and o Aql (F8V, $v_r = 1.40$ kms^{-1}) with the same instrumental

[1]http://www.tug.tubitak.gov.tr/rtt150_tfosc.php

set-up. The spectra of these two stars were used as templates for radial velocity determinations and preliminary spectral type estimations. Typical signal-to-noise ratios (SNR) of observed spectra are between 140 and 190 for a single observation with an hour of exposure time.

We reduced and extracted the observed spectra by following standard steps for reducing and extracting échelle spectra. In the first step, bias correction was applied to all images, and a normalized flat-field image was obtained via bias-corrected halogen lamp frames. Then, all science and Fe-Ar calibration frames were divided by the normalized flat-field frame; scattered light correction was applied to all bias and flat-field corrected images. At that point, reduced science and Fe-Ar images were obtained. Next, spectra were extracted from the reduced images. In the following steps, wavelength calibration was applied to the reduced and extracted science frames via Fe-Ar images, and finally wavelength calibrated science images were normalized to the continuum by using cubic spline functions. The whole procedure was applied under IRAF[2] environment.

2.2. *Photometric Data*

In the light curve and $O-C$ analyses, we mainly use long cadence (29.4 minutes of exposure time, hereafter LC) Kepler photometry, which is available in the Kepler eclipsing binary catalogue[3] as detrended and normalized fluxes (Slawson et al. 2011; Prša et al. 2011). We also use the short cadence (hereafter SC) data from the same database in the same format, in order to investigate possible high frequency variations. The data were collected over a broad wavelength interval between 4100Å and 9100Å, which suffers from lack of color information, but provides very high precision. The LC data cover ≈ 4 years of time base without any considerable time gap. The reported light contamination is 0.3% in the MAST database, practically meaning no light contribution of any light sources from the background. Available SC and LC photometry is shown in Figure 1. In the figure, we computed the phase-folded light curve with respect to the light elements in equation (1) given by Slawson et al. (2011).

[2]The Image Reduction and Analysis Facility is hosted by the National Optical Astronomy Observatories in Tucson, Arizona at iraf.noao.edu.

[3]http://keplerebs.villanova.edu/

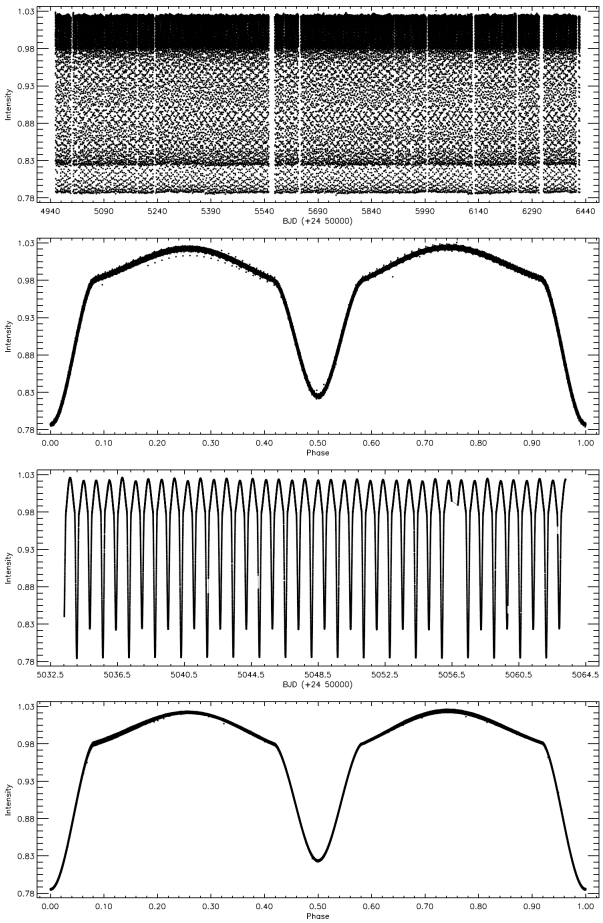

Fig. 1. KIC 8043961 light curve derived with the data taken from the Kepler Database. In the upper two panels, the light variation is plotted versus time and phase depending on available LC Data; it is plotted for the SC data in the bottom two panels.

3. ANALYSES AND MODELS

3.1. *Radial Velocities and Spectroscopic Orbit*

We start our analysis with the measurement of the radial velocities of each component, in order to determine the spectroscopic orbit of the system. For this purpose, we cross-correlate each observed spectrum of KIC 8043961 with spectra of ι Psc and o Aql. The cross correlation was applied according to the method proposed by Tonry and Davis (1979). The practical application of the method was done with the FXCOR task under IRAF environment. Among the two template stars, ι Psc provided a slightly better cross-correlation and was adopted as the radial velocity template. Cross-correlation was performed for the wavelength range between 4900 - 5400Å, ignoring strongly blended spectral lines. In Figure 2,

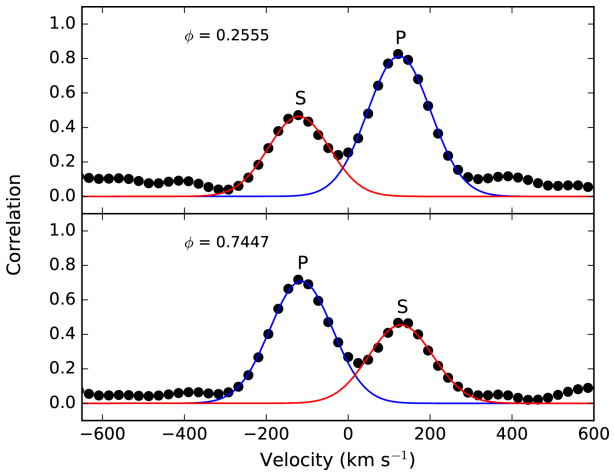

Fig. 2. Cross-correlation functions of KIC 8043961 obtained at orbital quadratures. The letter ϕ shows the orbital phase in each panel. P and S denote the primary and secondary component, respectively. The color figure can be viewed online.

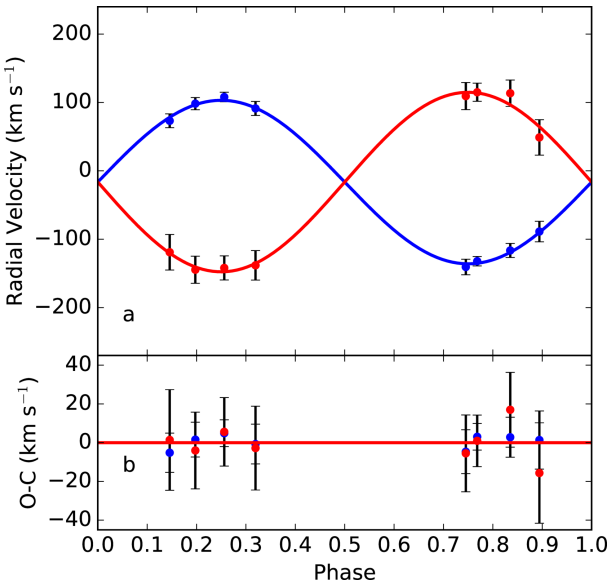

Fig. 3. (a) Measured radial velocities of the primary and the secondary component (blue and red filled circles, respectively), and corresponding model orbit (blue and red curve). (b) Residuals from the model. The color figure can be viewed online.

we show the cross-correlation functions of spectra obtained at orbital quadratures, where both components are clearly resolved.

We tabulate the measured radial velocities in Table 2, together with brief observational information. In the table, orbital phases are calculated via ephemeris time and period given by Borkovits et al. (2016). These light elements are adopted for phasing the radial velocities and light curve.

Before attempting an orbital solution, we inspected the orbital eccentricity via phased folded Kepler photometry. Primary and secondary eclipses are located precisely at 0.0 and 0.5 phases, respectively, indicating a non-eccentric orbit. Therefore, we model the spectroscopic orbit assuming a circular orbit. The orbital solution was achieved by applying the Levenberg-Marquardt algorithm (Levenberg 1944), and Markov Chain Monte Carlo simulations via EMCEE software developed under a Python environment (Foreman-Mackey et al. 2013). We tabulate the final spectroscopic orbit parameters and their uncertainties in Table 3, and we plot the phase-folded radial velocities, theoretical models and residuals from the best-fitting models in Figure 3. We notice that the less massive, smaller and hotter component is eclipsed at the primary minimum, hence we interpret the numerical values in Table 3 according to this finding.

3.2. *Spectral Type*

In order to estimate atmospheric properties of the components reliably, we use the TFOSC spectrum of KIC 8043961 obtained at HJD 2456842.3645, corresponding to $\approx$ 0.75 orbital phase, where we can clearly resolve spectral lines of both components. The SNR of that spectrum is around 170, based on photon statistics. Before searching for the best atmospheric parameters, we fixed the micro-turbulence velocity of each component at 2 kms^{-1}, and the logarithm of the surface gravity $\log(g)$ of the primary and secondary components at 4.04 and 3.77, respectively. These $\log(g)$ values are calculated from combination of spectroscopic orbit parameters and light curve modeling results (see next section). Then we adjusted effective temperatures and metallicities of the components via the spectral synthesis method in a wavelength interval 4750 - 5750Å. In practice, we used the latest version of the Python framework *iSpec* (Blanco-Cuaresma et al. 2014). Synthetic spectra were calculated for temperatures between 6250 - 7250 K with steps of 50 K, and for metallicities between solar (0.0) and −1.0 with steps of 0.25. Among the different radiative transfer code options provided by *iSpec*, we adopted SPECTRUM[4] code

[4]http://www.appstate.edu/~grayro/spectrum/spectrum.html

TABLE 2

SPECTROSCOPIC OBSERVATIONS AND RADIAL VELOCITIES

HJD (24 00000+)	Orbital Phase	Exposure time (s)	Primary V_r km s^{-1}	Primary σ km s^{-1}	Secondary V_r km s^{-1}	Secondary σ km s^{-1}
56842.3645	0.7447	3000	−140.6	11.3	109.3	19.8
56842.4005	0.7678	3000	−132.1	6.9	115.0	13.3
56846.3781	0.3188	3000	91.3	10.3	−138.1	21.6
56888.2869	0.1970	3000	98.3	9.0	−144.6	19.8
56891.4965	0.2555	3000	108.0	6.9	−141.9	17.7
57592.4858	0.8344	1200	−116.4	10.3	113.5	19.3
57616.3579	0.1448	3600	73.2	10.1	−119.0	26.0
57854.5254	0.8934	2700	−88.7	15.0	48.9	25.9

TABLE 3

SPECTROSCOPIC ORBITAL ELEMENTS OF KIC 8043961*

Parameter	Value
$P_{\rm orb}$ (days)	1.5592121 (fixed)
T_0 (HJD2454+)	954.555903 (fixed)
γ (km s^{-1})	-15.4 ± 3
K_1 (km s^{-1})	131 ± 7
K_2 (km s^{-1})	120 ± 3
e	0 (fixed)
ω	...
$a \sin i$ ($R_\odot$)	7.7 ± 0.2
$M \sin^3 i$ ($M_\odot$)	2.56 ± 0.18
Mass ratio ($q = M_2/M_1$)	1.09 ± 0.07
rms1 (km s^{-1})	3.4
rms2 (km s^{-1})	8.9

*M_1 and M_2, masses of the primary and secondary component, M the total mass of the system.

(Gray and Corbally 1994) along with ATLAS9 model atmospheres (Castelli and Kurucz 2004) and a line list obtained from the third version of the Vienna atomic line database (VALD3) (Ryabchikova et al. 2015).

All calculated synthetic spectra were convolved with a Gaussian line spread function to match their resolution to the TFOSC spectra. After we obtained the instrumentally broadened synthetic spectra, we started to calculate the composite spectrum of the system. At that point, we selected a trial synthetic spectrum for the primary component. Next, we selected a synthetic spectrum for the secondary component, with a proper temperature as indicated by the preliminary light curve modelling. Then, we applied a proper radial velocity shift to each selected synthetic spectrum to match its spectral lines to the lines of the corresponding component in the observed spectrum. Finally, we calculated the composite spectrum of the system via synthetic spectra mentioned above, and the radius ratio, $R_1/R_2 = r_1/r_2 = 0.69$, where r means fractional radius, found from the light curve analysis. We repeated this process for every possible synthetic spectra configuration and searched the best matched composite spectrum of the system, i.e. the best–fitting synthetic spectrum for each component. We checked the reliability of the parameters suggested by the best matched synthetic spectra, with the best-fitting light curve model parameters. Confirming the light curve and spectroscopic modelling results iteratively, we find the self-consistent effective temperature of the primary and the secondary component as 6900 K and 6600 K. The temperatures and the surface gravities suggest F3V and F5 III-IV spectral types for the hot and cool components, respectively (Gray 2005). The resulting overall metallicity of the system is found to be $[M/H] = 0.25$. Estimated uncertainties are 200K in temperature and -0.25 in metallicity, which are predicted by considering the temperature and metallicity steps in the model atmospheres, the SNR of observed spectra and the instrumental resolution of TFOSC spectra.

Furthermore, we observe a perceivable effect of rotational broadening in our spectra. Full width at half-maximum (FWHM) of the instrumental profile of TFOSC spectra is ≈1.8Å around 5500 Å, meaning that any projected rotational velocities ($v \sin i$) above ≈ 50 km s^{-1}could be observed. From the combined spectroscopic orbit and light curve modelling, we estimate $v \sin i$ values of the primary and the secondary component as 81 km s^{-1}and 54 km s^{-1}, respectively, assuming synchronous rotation. Since numerical fitting attempts of $v \sin i$ velocities did not

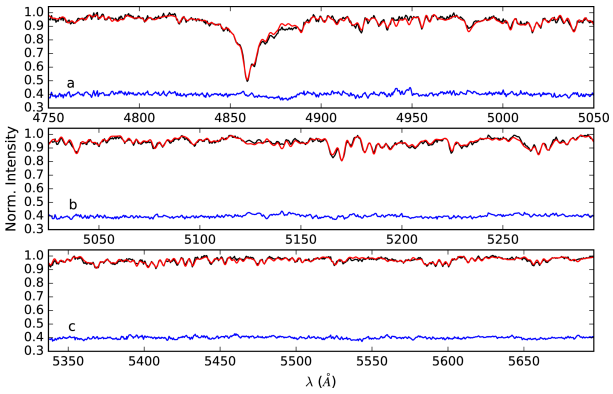

Fig. 4. Observed spectrum (black line), best-fitting composite synthetic spectrum (red line) and residuals (blue line). Residuals are shifted upwards by 0.4 for a better view. The color figure can be viewed online.

TABLE 4

TIMES OF MINIMA AND $O-C$ RESIDUALS*

MJD (Obs)	E	Type	O-C (II) (day)
54953.77420	−0.5	II	−0.00141
54954.55380	0.0	I	−0.00142
54955.33380	0.5	II	−0.00103
54956.11340	1.0	I	−0.00103
54956.89260	1.5	II	−0.00144
54957.67220	2.0	I	−0.00145
54958.45190	2.5	II	−0.00135
54959.23150	3.0	I	−0.00136
54960.01120	3.5	II	−0.00127
54960.79080	4.0	I	−0.00127

*Obtained from the Kepler SC and LC data.

yield stable and reliable results, we only applied rotational broadening to the corresponding synthetic spectrum of the components, by using the estimated velocities above, and then calculated the composite spectrum of the system. In Figure 4, we plot observed spectrum, best fitting composite synthetic spectrum and residuals.

3.3. *Orbital Period Variation*

In order to study the orbital period variation of KIC 8043961, we determine mid-times of primary and secondary eclipses, where we obtain 1688 minima times in total, of which 844 are the primary minima and 844 the secondary times of minimum. For each minimum, we only consider the orbital cycle that includes the corresponding minimum, and

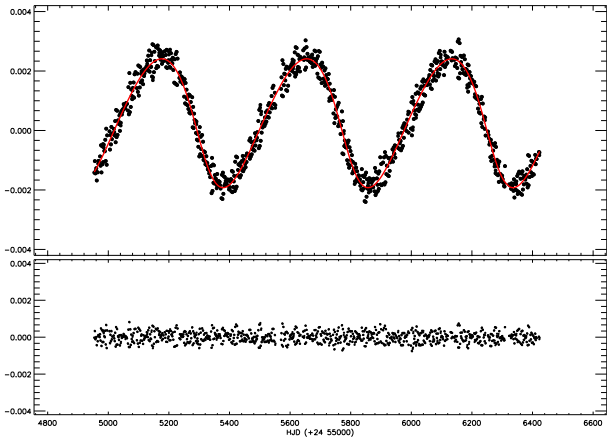

Fig. 5. The O-C variations of KIC 8043961. In the figure, the (O-C) II variation, derived after the linear correction, is shown in the upper panel, together with the best-fitting orbit (smooth red curve), while the residuals are shown in the bottom panel. The color figure can be viewed online.

then run the differential correction program of the Wilson-Devinney code by only adjusting ephemeris time and keeping all other parameters fixed. This process is fairly straightforward for primary eclipses, while we need to change the role of the components during the iterations, in order to compute secondary eclipses. Ten computed minima times are listed in Table 4, while the rest of them are available upon request. For each observed eclipse time, we compute expected eclipse times by using the following light elements (equation 1) to obtain $O-C$ values:

$$JD\ (Hel.) = 24\ 54954.555903\ +\ 1^d.5592121\ \times\ E. \quad (1)$$

Inspecting the $O-C$ values, we notice a clear sinusoidal variation, which is presumably due to the light travel time effect (hereafter LTTE) caused by an unseen third body in the system. Taking the light elements given in equation (1) as initial values, we modelled the sinusoidal variation together with the linear trend. Corrected ephemeris time and period are given by equation (2):

$$JD\ (Hel.) = 24\ 54954.555221(1) + 1^d.5592129(1) \times E + \Delta t, \quad (2)$$

where Δt is term for the LTTE of the third body. Using the corrected ephemeris time and the period, we calculate $(O-C)_{II}$ residuals. Applying the LTTE equation given by Irwin (1959) to the $(O-C)_{II}$ residuals, we calculate the orbit of the third body. In Figure 5, we show $(O-C)_{II}$ residuals together with

TABLE 5

THIRD BODY PARAMETERS OF KIC 8043961*

T_0	55311.00 ± 1.57
P (day)	478.339 ± 0.489
$a \sin i$ (AU)	0.387 ± 0.002
w (deg)	204 ± 1.11
e	0.266 ± 0.008
n	0.01314 ± 0.00001
$f(m)$	0.0337 ± 0.0035
M_3 ($M_\odot$)	4.909 (for $i = 15$ (deg)
M_3 ($M_\odot$)	1.161 (for $i = 45$ (deg)
M_3 ($M_\odot$)	0.799 (for $i = 75$ (deg)
M_3 ($M_\odot$)	0.767 (for $i = 90$ (deg)

*Derived from O-C analysis.

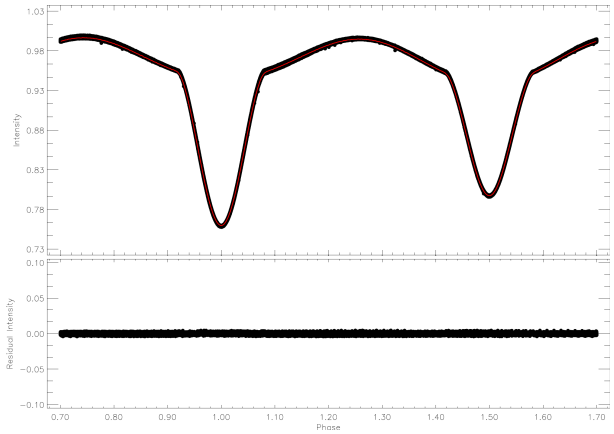

Fig. 6. Phase-folded LC light curve (filled circles) taken from the Kepler Database, and the best-fitting model (smooth red curve). The color figure can be viewed online.

the best-fitting third body orbit. Calculated third body parameters are listed in Table 5.

Assuming that the orbital inclination of the presumed third body is the same as the inclination of the eclipsing binary, and using the calculated total mass of the eclipsing binary (2.892 $M_\odot$) for the absolute parameters of the components, we estimated the mass of the third body as listed in Table 5 for different i values.

3.4. *Light Curve Analysis*

To determine the physical conditions of the components, we model the average SC light curve by using 2015 version of the Wilson - Devinney Code (Wilson and Devinney 1971; Wilson and Van Hamme 2014). The shape of the light curve clearly indicates a detached configuration. In the analysis, we fix the two critical parameters, mass ratio and effective temperature of the primary component (T_1) to 1.09 and 6900 K, respectively, which are found from the spectroscopic orbit modelling and the spectral type estimation. Considering the spectral type corresponding to this temperature, the albedos (A_1 and A_2) and the gravity-darkening coefficients (g_1 and g_2) of the components are adopted for the stars with convective envelopes (Lucy 1967; Rucinski 1969). The nonlinear limb-darkening coefficients (x_1 and x_2) of the components are taken from Van Hamme (1993). In the analyses, the temperature of the secondary component (T_2), the dimensionless potentials of the components (Ω_1 and Ω_2), the fractional luminosity of the primary component (L_1), the inclination of the system (i), the mass ratio of the system (q), the semi-major axis (a) and the third light are adopted as adjustable parameters. Although the synthetic curve derived by these parameters covers the entire observed light curve, a stable sinusoidal variation is still seen at out-of-eclipses. Considering the temperatures of the components, we modelled this variation by a stellar cool spot on the secondary component. We list the best-fitting model results in Table 6, and show the averaged phase-folded light curve together with the model in Figure 6.

The combination of results obtained from both the spectroscopic orbit and light curve modelling yields the physical parameters of the system listed in Table 7. These parameters show that the smaller, hotter and less massive primary component is still on the main sequence, while the larger, cooler and more massive secondary component appears to have evolved off the main sequence. We show the position of the components on the $\log(T_{\rm eff})$-$\log(L/L_\odot)$ plane in Figure 7. In the bottom panel of the figure, the evolutionary status of the components is shown in the same plane with isochrones for $[M/H] = -0.25$ (Bressan et al. 2012). The average age of the system is about 2.2 ± 0.3 Gyr.

3.5. *The Variation at Out-Of-Eclipses*

Inspecting the residuals from the light curve modeling, we find a clear signal of a sinusoidal variation at out-of-eclipses. Considering the place of the primary component of KIC 8043961 in the HR diagram, the source of the variation is possibly a γ Doradus type pulsation. We analyse the residual data to search for possible pulsation frequencies, using the PERIOD04 software (Lenz and Breger 2005) that is based on the

TABLE 6

LIGHT CURVE MODELLING RESULTS FOR KIC 8043961*

Parameter	Value
q	1.09 ± 0.07
i (°)	73.71 ± 0.02
T_1 (K)	6900 (fixed)
T_2 (K)	6598 ± 200
Ω_1	5.581 ± 0.003
Ω_2	4.432 ± 0.002
L_1/L_T	0.3450 ± 0.0005
L_2/L_T	0.6008
L_3/L_T	0.0542 ± 0.0012
g_1, g_2	0.32 (fixed), 0.457 ± 0.007
A_1, A_2	0.50 (fixed), 0.451 ± 0.003
x_1, x_2	0.654, 0.663 (fixed)
y_1, y_2	0.283, 0.274 (fixed)
$< r_1 >$	0.2261 ± 0.0001
$< r_2 >$	0.3286 ± 0.0002
Phase Shift	-0.000208 ± 0.000009
$Co - Lat_{SpotI}$ (rad)	1.519 ± 0.118
$Long_{SpotI}$ (rad)	1.808 ± 0.021
R_{SpotI} (rad)	0.183 ± 0.004
$T_{\rm fSpotI}$	0.98 (fixed)

*Internal uncertainty of T_2 is found as a few Kelvin, which is unrealistic, therefore it is assumed to be the same as the uncertainty of T_1.

TABLE 7

PHYSICAL PARAMETERS OF KIC 8043961

Parameter	Primary	Secondary
Mass ($M_\odot$)	1.379±0.109	1.513±0.181
Separation ($R_\odot$)	8.06±0.27	
Radius ($R_\odot$)	1.806±0.084	2.611±0.059
$\log L$ ($L_\odot$)	0.833±0.004	1.075±0.002
$\log g$ (cms^{-2})	4.06±0.01	3.78±0.03
M_{bol} (mag)	2.70±0.15	2.10±0.16

discrete Fourier transform (hereafter DFT) method (Scargle 1982). As seen in Figure 8, we found 137 frequencies which exceed the 3 σ level. We tabulate these frequencies in Table 8, and plot the resulting model obtained from these frequencies together with the residual light curve in Figure 9.

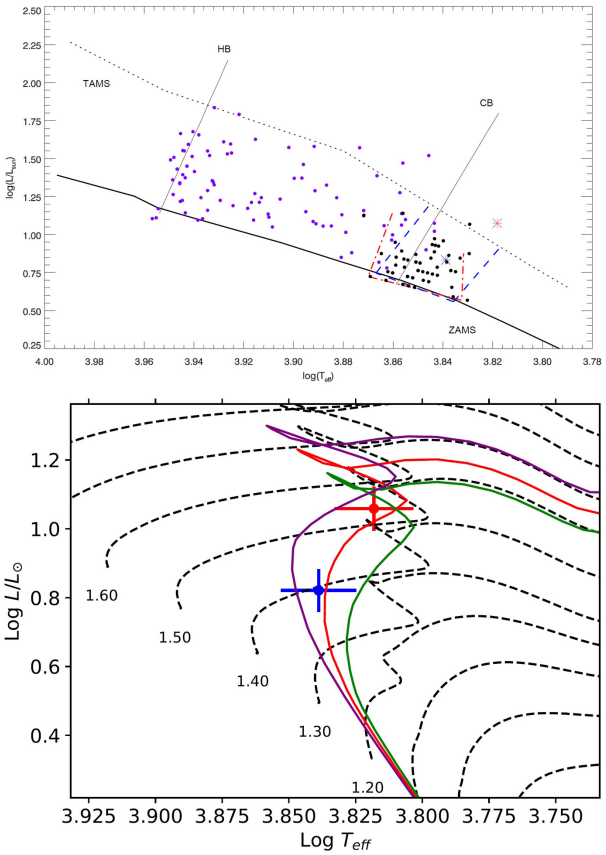

Fig. 7. Upper panel. Positions of the primary (blue asterisk) and the secondary (red asterisk) components of KIC 8043961 on the $\log(T_{eff})$-$\log(L/L_\odot)$ plane. The primary appears to be located among the γ Doradus type stars; the ZAMS and TAMS were taken from Girardi et al. (2000). The small filled black circles represent γ Doradus type stars listed in Henry et al. (2005). The dash-dotted lines (red) represent the borders of the area, in which γ Doradus stars appear. The blue dashed lines indicate the theoretical cool and hot boundaries of the γ Doradus instability strip, given by Warner et al. (2003). In addition, we plot the hot (HB) and cool borders (CB) computed from Rolland et al. (2002) of the δ Scuti stars for comparison. The small filled purple circles represent detached and semi-detached binaries taken from Soydugan et al. (2006). Bottom panel. Individual components in the same plane with three different isochrones (Bressan et al. 2012). The filled circle shows the less massive, smaller but hotter component, while the red filled circle shows the more massive, larger but cooler component. The green, red and purple isochrones are for $\log age$ of 9.40, 9.35 and 9.30, respectively. The color figure can be viewed online.

4. RESULTS AND DISCUSSION

Spectroscopic analysis and light curve modelling of KIC 8043961 reveal that the system is a slightly

TABLE 8

FREQUENCY LIST OF γ DOR PULSATION FOUND IN THE ANALYSIS*

Frequency	Frequency	Amplitude	Phase	Noise	SNR
F1	0.916416	0.000975	0.976502	0.000015	69.954572
F2	0.942190	0.000792	0.568788	0.000012	67.223506
F3	0.956949	0.000353	0.562851	0.000011	31.818026
F4	0.993697	0.000308	0.028697	0.000010	30.623664
F5	0.949851	0.000273	0.393345	0.000010	28.959837
F6	0.923608	0.000243	0.363458	0.000010	26.495071
F7	1.873358	0.000231	0.189382	0.000005	50.902279
F8	0.974498	0.000216	0.338794	0.000009	25.021613
F9	0.887055	0.000210	0.765381	0.000008	25.319987
F10	0.275072	0.000177	0.791680	0.000010	16.599333
F11	0.300848	0.000144	0.306613	0.000009	15.496189
F12	0.668357	0.000113	0.388377	0.000007	16.524546
F13	0.366276	0.000130	0.127347	0.000008	15.950863
F14	0.376595	0.000111	0.761279	0.000008	13.586635
F15	0.984063	0.000092	0.535489	0.000008	12.104475
F16	1.858608	0.000087	0.763904	0.000004	21.211509
F17	0.868183	0.000091	0.198983	0.000007	11.746275
F18	1.047241	0.000076	0.320245	0.000007	10.264264
F19	0.761510	0.000070	0.821559	0.000007	10.089111
F20	0.881004	0.000068	0.608747	0.000007	10.238665
F21	0.931190	0.000072	0.225136	0.000007	10.314234
F22	0.822440	0.000072	0.054409	0.000007	10.020085
F23	0.838783	0.000065	0.057601	0.000007	10.032803
F24	1.755210	0.000077	0.656801	0.000004	15.728606
F25	0.813057	0.000071	0.114027	0.000007	9.982051
F26	0.111354	0.000066	0.958094	0.000010	6.260455
F27	0.340336	0.000079	0.796978	0.000008	9.859690
F28	1.232040	0.000081	0.621758	0.000007	9.553888
F29	1.571022	0.000063	0.671356	0.000005	13.521431
F30	0.264255	0.000068	0.477712	0.000009	6.833383
F31	0.965094	0.000059	0.188122	0.000007	8.480951
F32	0.899936	0.000063	0.045391	0.000007	8.709595
F33	0.315615	0.000067	0.768945	0.000008	6.948675
F34	0.237268	0.000058	0.947569	0.000009	5.865668
F35	0.404073	0.000055	0.148505	0.000007	8.085690
F36	0.348656	0.000050	0.010840	0.000007	7.620083
F37	0.836521	0.000051	0.294970	0.000006	8.112678
F38	0.943443	0.000049	0.595186	0.000006	7.689664
F39	1.557797	0.000058	0.084863	0.000004	13.069212
F40	1.900344	0.000049	0.169896	0.000004	13.102947
F41	1.624016	0.000048	0.644379	0.000004	11.457698
F42	0.352339	0.000053	0.656969	0.000007	7.038268
F43	1.778928	0.000043	0.665775	0.000004	11.216445
F44	0.050852	0.000050	0.030521	0.000011	4.903525
F45	0.606112	0.000048	0.492856	0.000006	8.230251
F46	1.636105	0.000045	0.454696	0.000004	11.144403
F47	0.045897	0.000046	0.610881	0.000011	4.116043
F48	0.332966	0.000054	0.719763	0.000007	7.587804
F49	0.969087	0.000040	0.442950	0.000006	6.680742
F50	0.033530	0.000040	0.260326	0.000011	3.946902

*The frequency number is listed in the first column, the found frequency in the second column. The amplitude of the signal, its phase and the SNR value of the signal are listed in the following columns.

TABLE 8. CONTINUED

Frequency	Frequency	Amplitude	Phase	Noise	SNR
F51	0.041740	0.000047	0.429774	0.000011	4.078355
F52	0.062306	0.000037	0.493489	0.000010	4.169141
F53	0.923070	0.000043	0.116737	0.000006	7.247459
F54	3.848074	0.000041	0.054995	0.000002	26.143136
F55	0.875308	0.000042	0.639336	0.000006	6.855955
F56	0.899008	0.000044	0.795619	0.000006	7.304526
F57	0.035574	0.000044	0.888834	0.000011	3.755091
F58	0.893106	0.000039	0.673879	0.000006	6.583598
F59	0.071598	0.000043	0.565349	0.000010	3.878613
F60	1.217177	0.000035	0.448149	0.000006	6.225868
F61	1.113841	0.000039	0.919774	0.000006	6.361630
F62	0.084857	0.000036	0.273882	0.000010	3.841943
F63	0.862411	0.000036	0.413632	0.000006	6.209853
F64	0.308531	0.000042	0.978470	0.000007	5.737678
F65	0.039757	0.000037	0.482542	0.000010	3.592632
F66	0.086183	0.000044	0.204570	0.000010	3.904434
F67	0.028510	0.000036	0.522162	0.000010	3.593336
F68	0.037625	0.000033	0.879902	0.000010	3.707129
F69	0.066868	0.000036	0.694784	0.000010	3.749136
F70	0.833279	0.000034	0.689229	0.000006	6.115674
F71	1.935889	0.000034	0.797306	0.000003	10.342439
F72	0.046928	0.000033	0.926278	0.000010	3.641927
F73	0.752865	0.000032	0.937067	0.000006	5.713433
F74	0.282383	0.000036	0.613151	0.000007	4.667376
F75	0.072970	0.000028	0.029980	0.000009	3.490809
F76	0.810075	0.000034	0.929619	0.000006	5.908784
F77	1.040132	0.000031	0.368693	0.000006	5.415959
F78	1.583709	0.000039	0.872553	0.000004	9.394488
F79	0.118384	0.000038	0.211363	0.000009	3.530131
F80	0.122063	0.000033	0.274277	0.000009	3.576727
F81	0.044769	0.000031	0.735394	0.000010	3.384484
F82	0.805382	0.000030	0.060741	0.000006	5.294651
F83	0.780749	0.000031	0.365751	0.000006	5.371773
F84	1.020802	0.000027	0.375184	0.000006	5.185010
F85	0.846646	0.000030	0.693919	0.000006	5.545416
F86	0.043761	0.000034	0.107477	0.000009	3.412263
F87	0.034585	0.000039	0.200139	0.000010	3.459900
F88	0.245707	0.000031	0.792545	0.000007	4.078792
F89	0.067848	0.000035	0.019685	0.000009	3.554611
F90	0.359000	0.000035	0.418093	0.000006	6.172003
F91	0.088419	0.000031	0.117918	0.000009	3.347851
F92	0.049519	0.000031	0.486309	0.000009	3.294346
F93	0.063776	0.000033	0.104108	0.000009	3.338091
F94	2.562753	0.000026	0.981644	0.000003	8.832871
F95	1.050964	0.000028	0.679146	0.000006	5.069696
F96	0.120176	0.000027	0.035077	0.000008	3.521058
F97	1.832863	0.000027	0.560490	0.000003	8.258790
F98	0.054958	0.000026	0.032402	0.000009	3.240881
F99	0.818258	0.000029	0.418968	0.000005	5.095555
F100	0.032542	0.000031	0.505786	0.000009	3.299345
F101	0.061774	0.000029	0.393201	0.000009	3.545683
F102	2.304441	0.000028	0.820278	0.000003	9.129813
F103	1.916937	0.000027	0.628618	0.000003	8.333952
F104	1.017917	0.000028	0.195242	0.000006	4.844850

TABLE 8. CONTINUED

Frequency	Frequency	Amplitude	Phase	Noise	SNR
F105	0.122733	0.000029	0.432214	0.000008	3.368645
F106	0.950408	0.000028	0.602112	0.000005	5.224705
F107	0.821818	0.000027	0.269326	0.000005	4.904104
F108	0.841843	0.000026	0.694110	0.000005	4.802736
F109	0.829256	0.000026	0.364050	0.000005	4.815170
F110	1.924095	0.000026	0.710283	0.000003	8.248569
F111	1.803526	0.000026	0.101545	0.000003	7.742789
F112	0.110544	0.000026	0.860448	0.000008	3.174831
F113	0.121371	0.000028	0.336842	0.000008	3.299731
F114	0.667256	0.000026	0.971549	0.000005	5.183159
F115	1.085479	0.000025	0.856127	0.000005	4.717625
F116	0.078042	0.000026	0.774947	0.000008	3.147375
F117	0.139951	0.000025	0.056737	0.000008	3.302504
F118	0.879551	0.000025	0.330724	0.000005	4.705819
F119	0.325674	0.000030	0.500824	0.000006	4.975161
F120	0.289150	0.000028	0.489091	0.000006	4.504696
F121	0.097427	0.000026	0.330393	0.000008	3.024391
F122	0.183915	0.000024	0.516818	0.000007	3.389604
F123	0.679402	0.000023	0.754883	0.000005	4.665421
F124	0.785210	0.000024	0.650818	0.000005	4.493476
F125	0.349622	0.000024	0.885464	0.000005	4.458943
F126	0.976807	0.000023	0.012797	0.000005	4.546269
F127	0.826710	0.000023	0.947968	0.000005	4.591718
F128	0.135705	0.000023	0.926925	0.000007	3.195712
F129	0.073810	0.000025	0.799563	0.000008	3.098061
F130	0.096326	0.000025	0.795353	0.000008	3.195557
F131	0.065866	0.000026	0.081159	0.000008	3.400311
F132	2.568079	0.000022	0.918795	0.000003	7.820700
F133	0.124682	0.000023	0.168908	0.000007	3.082160
F134	0.850509	0.000022	0.945916	0.000005	4.448453
F135	1.598305	0.000027	0.093608	0.000004	7.420767
F136	1.288222	0.000022	0.231931	0.000004	4.861027
F137	0.027343	0.000023	0.735913	0.000008	2.869449

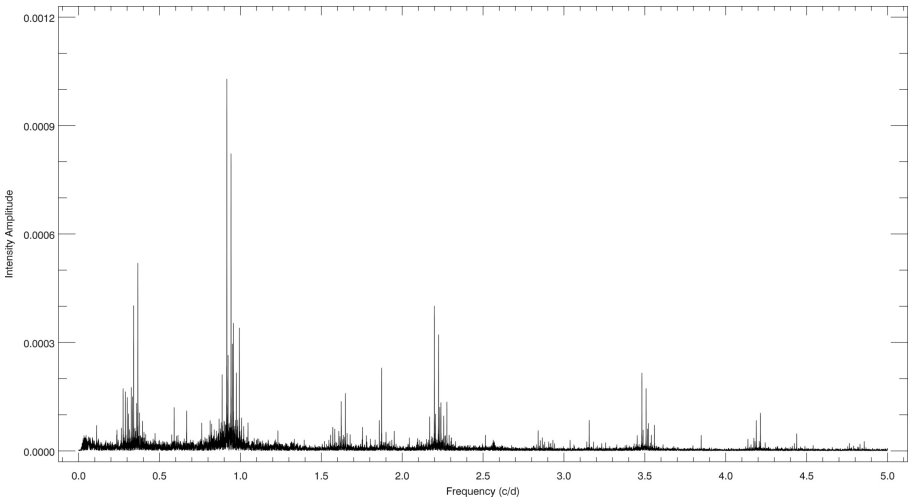

Fig. 8. KIC 8043961's Fourier amplitude spectrum derived from the DFT.

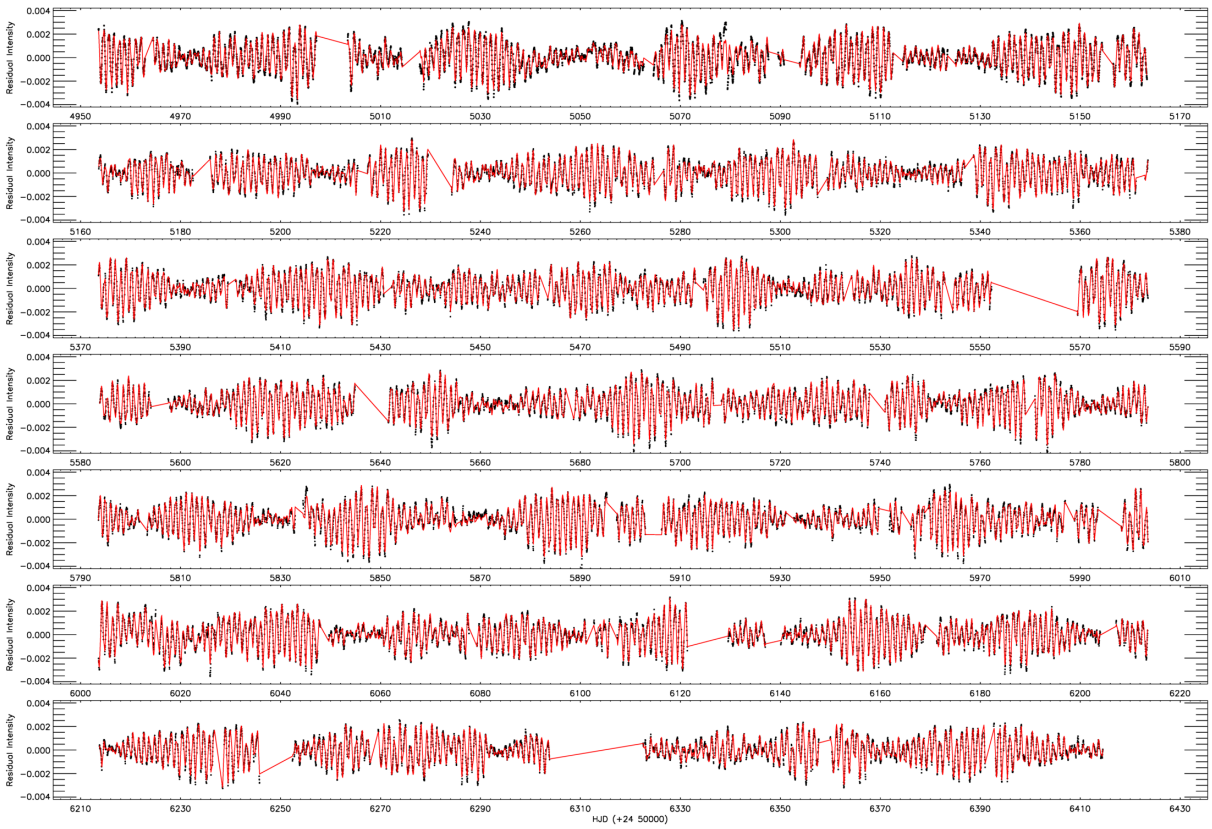

Fig. 9. The variation at out-of-eclipses and the synthetic model derived by the frequencies obtained from the DFT. The filled circles represent the observations, while the red line represents the model. The color figure can be viewed online.

metal-poor and detached eclipsing binary with a tertiary component. The eclipsing binary is composed of F3V and F5 III-IV stars, where the primary component is less massive and hotter than the evolved F5 III-IV secondary component. The average age of the system is found as 2.2 Gyr, based on PARSEC stellar evolutionary tracks and isochrones. Binary star evolution models must be considered for a more accurate age determination. The positions of the components on the $\log(T_{eff})$-$\log(L/L_{\odot})$ plane suggest that the primary is a γ Doradus type pulsator candidate. Inspecting the Fourier amplitude spectrum of the observed light variation at out-of-eclipses, we find 137 frequencies above the 3σ level. Most of the frequencies also confirm that one of the components is a γ Doradus type star.

Although Borkovits et al. (2016) computed the orbit of the tertiary component via eclipse time variation analysis, we re-compute eclipse times during the light curve modelling, and model the orbit of the third body via these eclipse times. We find very similar orbital parameters, except for the longitude of the periastron, which differs by 180 degrees from the value found by Borkovits et al. (2016). The difference is likely due to the different reference plane of the orbit; we adopt the definitions of Irwin (1959) but Borkovits et al. (2016) shift the reference plane of the orbit to the focal point of the ellipse.

Using the computed total mass of the eclipsing binary and assuming that the inclination of the third body orbit is the same as the inclination of the eclipsing binary, we find the mass of the third body to be about 0.778 $M_{\odot}$. However, we estimated the mass of the third body as listed in Table 5 for different inclination values. The mass of the third body was found to range from 4.909 $M_{\odot}$ for $i = 15$ deg to 0.767 $M_{\odot}$ for $i = 90$ deg. Considering the estimated masses of the primary and secondary components listed in Table 7 and also the value of L_3/L_T in Table 5, the acceptable mass should range from 0.799 $M_{\odot}$ for $i = 75$ deg to 0.767 $M_{\odot}$ for $i = 90$ deg. Assuming that the tertiary component is a main sequence star, this mass corresponds to the effective temperature of 4990 K (Tokunaga 2000).

We thank the referee for useful comments that have contributed to the improvement of the paper. We also wish to thank the Turkish Scientific and Technical Research Council (TÜBİTAK) for supporting this work through Grant No. 116F349 and for partial support in using the RTT-150 (Russian-Turkish 1.5-m telescope in Antalya) with Project Number 14BRTT150-667.

REFERENCES

Aerts, C., Christensen-Dalsgaard, J., & Kurtz, D. W. 2010, Asteroseismology, ed. W. B. Burton and V. Trimble (New York, NY: Springer), 49
Ammons, S. M., Robinson, S. E., Strader, J., et al. 2006, ApJ, 638, 1004
Balona, L. A. 2014, MNRAS, 437, 1476
_____. 2015, MNRAS, 447, 2714
Blanco-Cuaresma, S., Soubiran, C., Heiter, U., & Jofré, P. 2014, A&A, 569A, 111
Borkovits, T., Hajdu, T., Sztakovics, J., et al. 2016, MNRAS, 455, 4136
Borucki, W. J., Koch, D., Basri, G., et al. 2010, Sci, 327, 977
Bressan, A., Marigo, P., Girardi, L., et al. 2012, MNRAS, 427, 127
Caldwell, D. A., Kolodziejczak, J. J., & Van Cleve, J. E. 2010, ApJL, 713, 92
Castelli, F. & Kurucz, R. L. 2004, New Grids of ATLAS9 Model Atmospheres, (eprint arXiv:astro-ph/0405087), Available as Poster A20 on the CD-ROM which is part of the Proceedings of the IAU Symp. No 210; IAU Symp. No 210, IAUS 210, Modelling of Stellar Atmospheres, eds. N. Piskunov et al. 2003, poster A20
Conroy, K. E., Prša, A., Stassun, K. G., et al. 2014, AJ, 147, 45
Cunha, M. S., Aerts, C., Christensen-Dalsgaard, J., et al. 2007, A&ARev., 14, 217
Foreman-Mackey, D., Hogg, D. W., Lang, D., & Goodman, J. 2013, PASP, 125, 306
Frasca, A., Molenda-Żakowicz, J., De Cat, P., et al. 2016, A&A, 594, 39
Girardi, L., Bressan, A., Bertelli, G., & Chiosi, C. 2000, A&AS, 141, 371
Gray, D. F. 2005, The Observation and Analysis of Stellar Photospheres, 3rd ed., (Cambridge, MA: CUP)
Gray, R. O. & Corbally, C. J. 1994, AJ, 107, 742
Grigahcène, A., Antoci, V., Balona, L., et al. 2010, ApJ, 713, 192
Henry, G. W., Fekel, F. C., & Henry, S. M. 2005, AJ, 129, 2815
Huber, D., Silva Aguirre, V., Matthews, J. M., et al. 2014, ApJS, 211, 2
Irwin, J. B. 1959, AJ, 64, 149
Jenkins, J. M., Caldwell, D. A., Chandrasekaran, H., et al. 2010a, ApJ, 713, 87
Jenkins, J. M., Chandrasekaran, H., McCauliff, S. D., et al. 2010b, SPIE, 7740, 77400
Kamil, C. & Dal, H. A. 2017, PASA, 34, 29
Kirk, B., Conroy, K., Prša, A., et al. 2016, AJ, 151, 68
Koch, D. G., Borucki, W. J., Basri, G., et al. 2010, ApJ, 713, 79
Lenz, P. & Breger, M. 2005, CoAst, 146, 53
Levenberg, K. 1944, QApMa, 164
Lucy, L. B. 1967, ZA, 65, 89
Mathur, S., Huber, D., Batalha, N. M., et al. 2017, ApJS, 229, 30
Matijevič, G., Prša, A., Orosz, J. A., et al. 2012, AJ, 143, 123
Özdarcan, O. & Dal, H. A. 2017, PASA, 34, 17
Pickles, A. & Depagne, É. 2010, PASP, 122, 1437
Pinsonneault, M. H., An, D., Molenda-Żakowicz, J., et al. 2012, ApJS, 199, 30
Prša, A., Batalha, N., Slawson, R. W., et al. 2011, AJ, 141, 83
Rolland, A., Costa, V., Rodríguez, E., et al. 2002, CoAst, 142, 57
Ruciński, S. M. 1969, A&A, 19, 245
Ryabchikova, T., Piskunov, N., Kurucz, R. L., et al. 2015, PhyS, 90, 4005
Scargle, J. D. 1982, ApJ, 263, 835
Slawson, R., Prša, A., Welsh, W. F., et al. 2011, AJ, 142, 160
Soydugan, E., Soydugan, F., Demircan, O., & İbanoğlu, C. 2006, MNRAS, 370, 2013
Tkachenko, A., Aerts, C., Yakushechkin, A., et al. 2013, A&A, 556, 52
Tokunaga, A. T. 2000, in Allen's Astrophysical Quantities, ed. A. N. Cox (4th ed.; New York, NY: Springer) 143
Tonry, J. & Davis, M. 1979, AJ, 84, 1511
Uytterhoeven, K., Moya, A., Grigahcène, A., et al. 2011, A&A, 534, A125
Van Hamme, W. 1993, AJ, 106, 2096
Warner, P. B., Kaye, A. B., & Guzik, J. A. 2003, ApJ, 593, 1049
Watson, C. L., Henden, A. A., & Price, A. 2006, SASS, 25, 47
Wilson, R. E. & Devinney, E. J. 1971, ApJ, 166, 605
Wilson, R. E. & Van Hamme, W. 2014, ApJ, 780, 151

H. A. Dal, C. Kamil, O. Özdarcan, and E. Yoldaş: Department of Astronomy and Space Sciences, University of Ege, Bornova, 35100 İzmir, Turkey (ali.dal@ege.edu.tr).